Sequential fragmentation/transport theory, pyroclast size–density relationships, and the emplacement dynamics of pyroclastic density currents — A case study on the Mt. St. Helens (USA) 1980 eruption

Chelsea Mackaman-Lofland [a,*], Brittany D. Brand [a,b], Jacopo Taddeucci [c], Kenneth Wohletz [d]

[a] Department of Earth and Space Sciences, University of Washington, Seattle, WA 98195, USA
[b] Department of Geosciences, Boise State University, Boise, ID 83725, USA
[c] Instituto Nazionale di Geofisica e Vulcanologia, Rome, Italy
[d] Los Alamos National Laboratory, Los Alamos, NM 87545, USA

A B S T R A C T

Pyroclastic density currents (PDCs) are the most dangerous hazard associated with explosive volcanic eruptions. Despite recent advancements in the general understanding of PDC dynamics, limited direct observation and/or outcrop scarcity often hinder the interpretation of specific transport and depositional processes at many volcanoes. This study explores the potential of sequential fragmentation/transport theory (SFT; cf. Wohletz et al., 1989), a modeling method capable of predicting particle mass distributions based on the physical principles of fragmentation and transport, to retrieve the transport and depositional dynamics of well-characterized PDCs from the size and density distributions of individual components within the deposits. The extensive vertical and lateral exposures through the May 18th, 1980 PDC deposits at Mt. St. Helens (MSH) provide constraints on PDC regimes and flow boundary conditions at specific locations across the depositional area. Application to MSH deposits suggests that SFT parameter distributions can be effectively used to characterize flow boundary conditions and emplacement processes for a variety of PDC lithofacies and deposit locations. Results demonstrate that (1) the SFT approach reflects particle fragmentation and transport mechanisms regardless of variations in initial component distributions, consistent with results from previous studies; (2) SFT analysis reveals changes in particle characteristics that are not directly observable in grain size and fabric data; and (3) SFT parameters are more sensitive to regional transport conditions than local (outcrop-scale) depositional processes. The particle processing trends produced using SFT analysis are consistent with the degree of particle processing inferred from lithofacies architectures: for all lithofacies examined in this study, suspension sedimentation products exhibit much better processing than concentrated current deposits. Integrated field observations and SFT results provide evidence for increasing density segregation within the depositional region of the currents away from source, as well as for comparable density-segregation processes acting on lithic concentrations and pumice lenses within the current. These findings further define and reinforce the capability of SFT analysis to complement more conventional PDC study methods, significantly expanding the information gained regarding flow dynamics. Finally, this case study demonstrates that the SFT methodology has the potential to constrain regional flow conditions at volcanoes where outcrop exposures are limited.

© 2014 Elsevier B.V. All rights reserved.

1. Introduction

Pyroclastic density currents (PDCs) are ground-hugging currents of gas, ash, and pyroclasts that travel at high velocities down the flanks of volcanoes (Francis, 1993; Sparks et al., 1997). PDCs are the most dangerous hazard associated with explosive volcanic eruptions, but

because of current opacity and the risk inherent to observing PDCs in real time, the controls on transport and depositional processes are poorly understood. Volcanologists analyze PDC deposits to reconstruct flow characteristics. The flow information inferred from the study of PDC deposits is used to establish primary controls on runout distance, dynamic pressure, and other hazardous aspects of these currents (e.g., Valentine, 1998; Calder et al., 2000; Allen, 2001; Bourdier and Abdurachman, 2001; Dellino et al., 2011). However, outcrop exposure is often incomplete, and the extent to which local depositional characteristics are representative of the parent current transport and depositional processes

* Corresponding author.
E-mail address: chelsm42@outlook.com (C. Mackaman-Lofland).

at given spatial and temporal locations is still uncertain (e.g., Druitt, 1995; Giordano, 1998; Wohletz, 1998; Taddeucci and Wohletz, 2001; Branney and Kokelaar, 2002; Taddeucci and Palladino, 2002).

For this study, our objectives are to find and test methods that link PDC deposit characteristics with parent flow dynamics. We examine the solid fraction of PDCs, which is made up of discrete components including juvenile pumice and vitric glass fragments, accidental lithics, and free crystals. During both regional transport (i.e., transport from the PDC source to the depositional site) and local deposition, the components are preferentially sorted as a function of their size, density, and shape characteristics, resulting in particle distributions that can be identified at the outcrop scale (Wohletz et al., 1989; Calder et al., 2000; Taddeucci and Wohletz, 2001; Burgisser and Bergantz, 2002; Taddeucci and Palladino, 2002). We analyze the particle distributions in PDC deposits using sequential fragmentation/transport theory (SFT), a methodology that predicts mass distributions based on the physical principles of fragmentation and transport (Wohletz et al., 1989).

2. Field location: Mt. St. Helens

The MSH eruption began on the morning of May 18th with the collapse of the bulging edifice and subsequent debris avalanche. The debris avalanche was followed by a lateral blast that resulted from the decompression and rapid expansion of magma beneath the collapsed edifice (Kieffer, 1981; Fisher, 1990). The Plinian eruption that commenced after the blast continued throughout the day, reaching the climactic
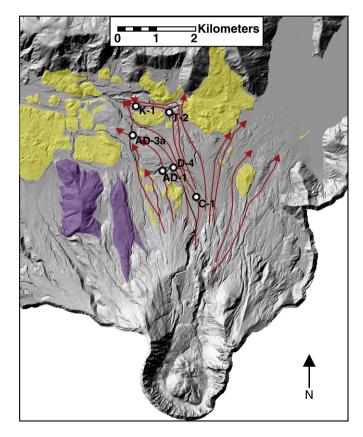

Fig. 1. LiDAR image of the Mt. St. Helens crater and pumice plain. The regions highlighted purple indicate pre-1980 eruption topography, and the regions highlighted yellow indicate exposed debris avalanche hummock deposits. Red arrows indicate dominant flow direction for Units III and IV as interpreted based on field observations and deposit characteristics. Outcrop names and locations are indicated; drainages and outcrops correlate with those described in Brand et al. (in press).

phase in the late afternoon (Christiansen and Peterson, 1981; Rowley et al., 1981; Criswell, 1987). The increase in eruptive intensity through the early afternoon and during the climactic phase produced multiple PDCs generated by column collapse events, which buried the area north of the crater under 10s of meters of PDC deposits (the present-day pumice plain; area with red arrows in Fig. 1).

Deep drainage erosion over the past 30 yr has provided kilometers of excellent exposure through the MSH deposits, allowing a detailed study of deposit structures to be conducted (cf. Pollock and Brand, 2012; Pollock, 2013; Brand et al., in press). Readers are referred to Brand et al. (in press) for a detailed analysis and interpretation of each MSH flow unit and outcrop location. Here we restrict our descriptions to the general depositional features and trends that are relevant to our research. 'Proximal' refers to outcrops <5.25 km from the crater, 'medial' refers to outcrops 5.25–7.25 km from the crater, and 'distal' refers to outcrops >7.25 km from the crater. Lithofacies abbreviations are modified from Branney and Kokelaar (2002) and are presented in Table 1.

2.1. Mt. St. Helens PDC flow units

Four major PDC flow units are identified in the drainages that transect the pumice plain, which extends from the break in slope north of the MSH crater to Johnson Ridge (Figs. 1 and 2). We associate Units I and II with the waxing afternoon phase of the eruption (termed the early ash flow phase by Criswell, 1987), and Units III and IV with the climactic phase of the eruption (termed the climactic ash flow phase by Criswell, 1987).

Units I and II represent the first PDCs to traverse the MSH pumice plain. The base of Unit I is rarely exposed, but where observed it is in contact with debris avalanche and blast deposits from the beginning phases of the eruption. Overall, both Units I and II are thicker (>10 m) and dominated by massive lapilli tuff (mLT) in the distal regions, and thinner (<6 m) and dominated by stratified (sLT) to diffusely-stratified and diffusely cross-stratified (dsLT) deposits in the medial distances (Table 1). Both flow units grade between mLT, dsLT, and sLT over short vertical and lateral distances (vertical gradations occur within meters; lateral gradations over 10s–100s of meters), and the deposits generally become finer grained and have tighter sorting with distance from source (see Fig. 4 in Brand et al., in press). Pumice lenses are common in both flow units and increase in abundance in the distal regions. The contacts between Units I and II, and between Units II and III, are characterized by thin (<50 cm), somewhat laterally continuous massive tuffs.

The massive nature and general lack of fabric within the distal deposits suggests that they were produced by a concentrated current with negligible shear stress. However, the proximal stratified and diffusely-stratified deposits indicate depositional regions where traction and/or granular flow boundaries occurred, likely as a consequence of variability in surface roughness, and reflect the inherent unsteadiness within the currents that produced Units I and II. The laterally continuous and massive nature of the fine ash layer between the units suggests that deposition occurred via direct fallout (cf. Branney and Kokelaar, 2002). Thus we interpret that the fine ash layers settled from a co-ignimbrite ash cloud, the waning tail of the current, or some combination of the two.

Table 1
Lithofacies symbols (modified from Branney and Kokelaar, 2002).

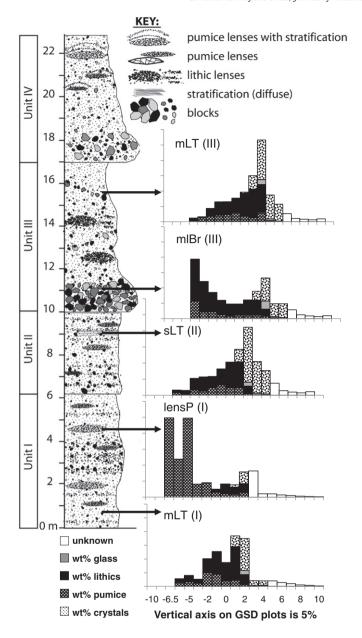| Symbol	Lithofacies
mLT	Massive lapilli tuff
mlBr	Massive lithic breccia
sLT	Stratified lapilli tuff
xsLT	Cross-stratified lapilli tuff
dsLT	Diffuse stratified lapilli tuff
lensP	Pumice lens

Fig. 2. Generalized stratigraphic column for the four major PDC flow units produced during the May 18th, 1980 Mt. St. Helens eruption. Histograms provide example grain size distribution (GSD) and componentry data for massive lapilli tuff (*mLT*), lithic breccia (*mlBr*), stratified lapilli tuff (*sLT*), and pumice lens (*lensP*) samples obtained from outcrop AD-3.

accumulations sometimes reveal a diffuse fabric, although this is not pervasive across the flow unit. There is no obvious decrease in the Unit III median grain size or increase in degree of sorting with distance from source (see Fig. 4 in Brand et al., in press). Pumice lenses are not present in Unit III, and the Unit III deposits are not fines depleted. The negligible fines depletion (and therefore lack of evidence for ash elutriation), weak segregation of lithics, and lack of obvious pumice segregation suggest that the deposits were produced by a highly concentrated current with suppressed size-density segregation (Druitt, 1995; Druitt et al., 2007). The general absence of fabric suggests low basal shear rates that locally and temporally increase to produce the rarely-observed diffuse block fabric (Unit III lateral facies variations visible in Fig. 3).

Unit IV is typically finer-grained than Units I–III, and develops tighter sorting with distance from source (Brand et al., in press). The blocks of Unit IV are most often found as concentrated lithic breccias at the base of the flow unit or dispersed within the first few meters above the base of the unit (Figs. 2 and 3). Pumice lenses are common in Unit IV and increase in abundance in the distal regions. The massive nature, basal accumulation of lithic blocks, and abundant pumice lenses suggest that Unit IV was deposited from the base of a concentrated, density stratified current with negligible basal shear stress. The even thicknesses of Units III and IV across the depositional area and the extensive runout distances observed (up to 9 km) suggest that both units were deposited by highly mobile currents. This evidence, combined with the massive characteristics, high ash content, and general lack of fabric within the deposits, suggests that the currents were fluidized and maintained high internal pore pressure across much of the runout distance (cf. Roche, 2012).

2.2. Research objectives

The excellent vertical and lateral PDC deposit exposure at MSH offers a unique opportunity to test the applicability of using size–density relationships and physical parameters to describe component particle distributions and decipher local versus regional transport processes. This study seeks to determine (1) to what degree SFT analysis of particle fragmentation and transport mechanisms is influenced by variations in the initial component distributions of target pyroclastic deposits, (2) how the results of SFT analysis compare with conventional PDC study methods when examining the impact of travel distance on the deposit characteristics of a single PDC flow unit, and (3) the extent to which size–density relationships and SFT analysis can be used to reconstruct flow boundary conditions and emplacement mechanisms for a variety of PDC lithofacies. We additionally combine field observations with SFT results in order to obtain further information regarding PDC dynamics within the flow boundary zone.

3. Methods

3.1. Grain size, componentry, and density methods

For each sample we collected grain size data from −8 ϕ to 8 ϕ. Scaled photographs were analyzed to determine the percent of clasts <−6 ϕ. Grain sizes between −6 ϕ and −3 ϕ were sieved in the field, and medium grain sizes (−3 to 2 ϕ) were dried and sieved in the lab. All sieving was conducted at one-ϕ intervals using standard sieve techniques. The finest fraction (>2 ϕ) was analyzed using a MicroTrak laser grain size instrument.

As defined in Branney and Kokelaar (2002), "fines depletion" refers to deposits that contain a lesser amount of ash than the surrounding PDC deposits. To determine the relative quantity of fine ash in the MSH deposits, we follow the methods of Walker (1983) and compare the sample weight percent of ash smaller than 0 ϕ (1 mm; F1) with the weight percent of ash smaller than 4 ϕ (1/16 mm; F2). Ash smaller than 4 ϕ is most susceptible to elutriation, so calculating the F2:F1 ratio

The climactic phase of the eruption produced the most voluminous and wide-spread PDCs, which are responsible for the massive, lithic block-rich Units III and IV. These units are more widely exposed than Units I and II, with excellent outcrops proximal to distal from source (Fig. 2). Unit III often has an erosive contact with scours that extend into the underlying flow unit (Unit II). Where not erosive, the contact between Units II and III is denoted by a fines-rich massive tuff similar to that found between Units I and II. The contact between Units III and IV varies from sharp with a thin massive tuff at the contact, to diffuse and unrecognizable.

Units III and IV are block-rich, poorly-sorted massive lapilli tuffs. They are evenly distributed across the pumice plain, and have thicknesses up to 9.5 and 8 m, respectively. The blocks of Unit III are found in lithic breccias (*mlBr*; Table 1) close to the base of the flow unit, in lithic lenses dispersed throughout the thickness of the deposit, or as individual lithics randomly dispersed throughout the deposit. Block
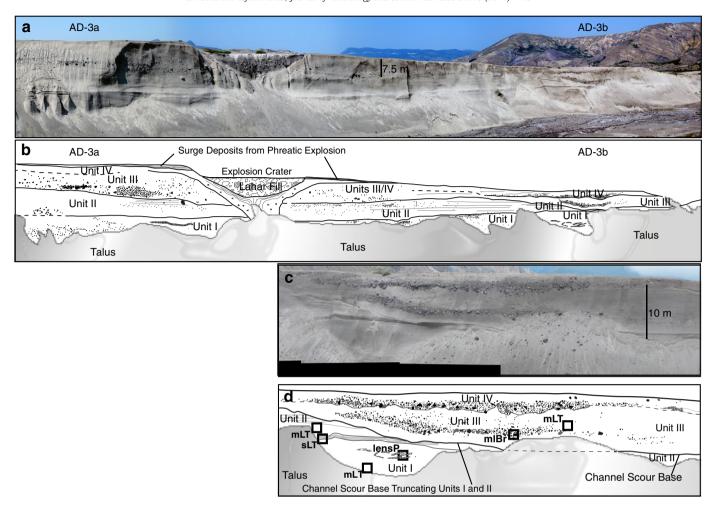
Fig. 3. (a) Photograph of the AD-3 outcrop, PDC travel distance estimated to be ~7.18 km from source. (b) Sketch of the AD-3 outcrop with lithofacies, depositional features, and flow units outlined and labeled. (c) Close-up photograph of the erosional lithic levees on the north side of the outcrop; (d) sketch of the levee features with lithofacies and flow units denoted. Boxes indicate sample locations for this study.

enables the observation of relative fines enrichment or depletion in the PDC deposits (Walker, 1983). For the data spread at MSH, F2:F1 ratios ≤1.6:10 are considered "fines-depleted" and ratios ≥3.5:10 are considered "fines-enriched."

Juvenile pumice, free crystals, and accidental lithic components were distinguished for each grain size. We separated the components by hand picking down to 4 ϕ (a binocular microscope was used for phi sizes >0 ϕ). Due to the difficulty of accurately separating the three components for grain sizes smaller than 4 ϕ, we determined the componentry of the finest size bins using a scanning electron microscope (SEM). Consistent with assumptions made in the literature, MSH grain sizes >4 ϕ are predominantly made up of crystals and crystal fragments (Sparks, 1976). We also observe a fraction of glass particles derived from fragmented pumices that are present in this size class; however, due to the extremely small proportion of glass and the physical difficulty of separating glass and crystal fragments in this size range, the glass component is not included in this study. To ensure the accuracy of the component distributions, we calculated the relative % (in number of particles) of each component after a 100, 300, 500, and 1000 particle count for several samples. This accuracy study indicated that a 300 particle count for each grain size is accurate to within 5% (slightly greater error for grain sizes ≤0 ϕ); the component percentages presented in this study were determined using particle counts of at least 300 grains.

Density was calculated using water displacement methods for lithic and crystal components for grain sizes between −3 ϕ and 1 ϕ; water

displacement methods were applied to >300 clasts for each component grain size. During water displacement we observed that closest packing for lithics and crystals results in ~50% particle void space. To calculate the pumice density we measured the weight of each sample, and assume 50% void space between pumice clasts to determine the pumice sample volume. We use these weight and assumed volume values to calculate MSH pumice density for the −3 ϕ to 1 ϕ size range. A secondary density study was conducted for the 1 ϕ grain size using a helium picnometer to determine sample volume and void space for the lithic and crystal components (the pumice vesicularity resulted in inaccurate picnometer volume measurements). The water displacement and helium picnometer methods produce consistent density results. We average the density measurements of each component, and use the resulting values to convert particle size–frequency diagrams from volume to weight proportions (Fig. 2).

3.2. Sequential fragmentation/transport theory

PDC component grain size distributions are described using sequential fragmentation/transport theory (SFT). SFT analysis is a methodology that predicts particle mass distributions through integration of a sequence of fragmentation and transport events, parameterized by an initial mass distribution and the mass sensitivities of fragmentation and transport processes (Brown and Wohletz, 1995). Predicted SFT distributions are optimized to observed sample distributions in order to establish a forward model that best characterizes the sample. While

conventional methods have historically provided effective descriptions of size–frequency distributions, the methods (e.g., lognormal best-fit curves) are based on empirical characterizations of grain size data, and as such any physical interpretation is fundamentally limited (Sheridan et al., 1987; Wohletz et al., 1989; Wohletz, 1998). SFT applies to particle mass distributions that have undergone a sequence of fragmentation and transport events, and produces distribution models that are physically rather than empirically based (Wohletz et al., 1989). As such, SFT can be used to determine physical processes from distribution parameters. Additionally, previous studies indicate that model functions produced using SFT analysis fit the size–frequency curves of pyroclastic deposits more accurately than lognormal functions (Wohletz et al., 1989; Orsi et al., 1992; Wohletz and Raymond, 1993; Brown and Wohletz, 1995; Wohletz et al., 1995; Taddeucci and Palladino, 2002).

We apply the SFT software program developed by K. Wohletz (©KWARE, University of California 2000) to analyze the MSH data. This software allows user-interactive characterization of data subpopulations within complex, polymodal size distributions. For each sample, the bulk grain size distribution is decomposed into discrete component distributions, which are then analyzed individually using the SFT software. The program first fits a cubic spline curve to the grain size histogram. The operator then isolates distribution subpopulations, and characterizes each subpopulation by determining the approximate mode, standard deviation, and weight fraction for a representative SFT function. The operator is able to refine the synthetic SFT functions to create a best-fit composite curve for the original data spline (Fig. 4). Best-fit is determined by calculating the residual weight fraction between the original histogram spline and the synthetic composite curve. In cases where the MSH samples display clear data curve truncations, rather than discarding the data points we include approximate weight percent and componentry values in order to complete the curves and obtain representative functions and descriptive parameters.

SFT analysis characterizes the MSH component distributions using one to six data subpopulations, and describes the subpopulations in terms of three parameters: weight fraction, mode, and dispersion. *Weight fraction* expresses the relative proportion of a given subpopulation within the entire component sample. *Mode* is the phi size at the peak of a subpopulation. *Dispersion* is directly related to the mass sensitivity of the subpopulation fragmentation or transport mechanisms; larger dispersion values reflect increased particle processing through fragmentation and transport events. The dispersion parameter describes the shape of the synthetic size–frequency curve similar to the standard deviation for a lognormal curve, but SFT dispersion also controls a predicted amount of skewness. Dispersion values near −1 produce coarse, flat model distributions, while increasing values (reflecting more advanced particle processing) result in distributions that are fine-skewed and more peaked (Fig. 5). When plotted against each other, the weight fraction, mode, and dispersion parameters can be used to attribute the different subpopulations to specific particle
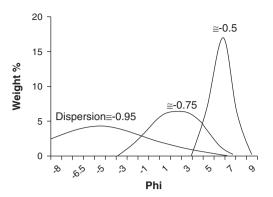

Fig. 5. Increasing values of the dispersion parameter used in SFT analysis. Values near −1 produce coarse, flat model distributions and reflect a lesser degree of particle processing, while greater dispersion values result in distributions that are peaked and fine-skewed, and reflect more advanced particle processing. Modeled after Wohletz et al. (1989) and Taddeucci and Palladino (2002).

transport and emplacement mechanisms (e.g., Wohletz et al., 1989; Orsi et al., 1992; Wohletz and Raymond, 1993; Wohletz, 1998). See Wohletz et al. (1989) for a complete description of the SFT software program and the mathematical derivation of the parameters.

4. Results

4.1. Grain size, componentry, and density results

Juvenile pumice, free crystals, and accidental lithic components were distinguished for each grain size. The juvenile MSH pumice clasts are characterized by approximately 30% phenocrysts, including plagioclase, orthopyroxene, amphibole, and iron–titanium oxide crystals, in a glassy groundmass with microlites (weight percent calculated vesicle-free to 100%; Kuntz et al., 1981). Comparison of the crystal size and mineralogy of both pumice and free crystals suggests that free crystals are almost entirely derived from fragmented pumices. A greater quantity of felsic crystals than mafic crystals are observed for all crystal size bins. Lithics are derived from past eruptive periods at MSH, and include basalt, basaltic andesite, andesite, dacite, and rhyodacite. Average pumice density was calculated to be 1300 kg m^{-3}, lithic density to 2700 kg m^{-3}, and crystal density to be 2600 kg m^{-3}. These average values were used to calculate component weight percent for each sample and create bulk and individual component distributions (Fig. 2).

4.2. SFT results

SFT descriptive parameters (weight fraction, mode, and dispersion) are plotted for the pumice, lithic, and crystal components of each sample. The *mode* versus *weight percent* plots allow us to determine the most representative SFT subpopulations for each component within a
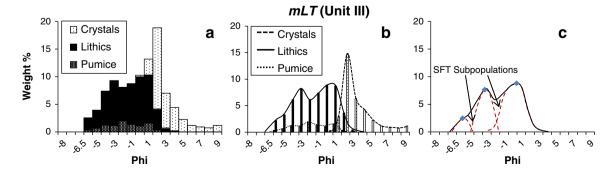

Fig. 4. (a) Decomposition of a combined grain size distribution (*mLT* sample from Fig. 3) into individual component distributions. (b) SFT analysis fits cubic spline curves to the component distributions, and then (c) characterizes the spline curves using a series of data subpopulations.

given sample. The *mode* versus *dispersion* plots characterize the degree of particle processing that the component subpopulations in the distribution have experienced. The *weight percent* versus *dispersion* plots show subpopulation particle processing trends that reflect the extent to which each data point represents the overall component distribution.

We use these plots to address our study questions. We compare the SFT parameter distribution trends observed (1) for three samples within the fallout lithofacies in order to assess the influence of variations in initial component distributions on SFT results (Fig. 6), (2) for a single PDC flow unit over changing distance from source to compare SFT results with those obtained using conventional PDC study methods (Fig. 7), and (3) across lateral facies variations that occur throughout multiple flow units to evaluate and constrain the ability of SFT analysis to reconstruct flow boundary conditions and emplacement mechanisms as indicated by fabric studies and deposit structures (Figs. 8–10). An objective analysis of the data trends is presented below in Sections 4.2.1 Fallout Data, 4.2.2 Travel Distance Data, and 4.2.3 Lithofacies Variation Data; interpretations are presented in Section 5 Discussion, and Subsections 5.1 Fallout, 5.2 Travel Distance, and 5.3 Lithofacies Variation.

4.2.1. Fallout data

We plot the SFT parameters describing the fallout samples separately from the other lithofacies to examine how the same transport process

affects parameter values of samples with varied component distributions. We collected three MSH fallout samples, each with a distinctly different relative component distribution (Table 2; grain size and componentry data courtesy of Benjamin Andrews, Smithsonian Institute). Sample B1_a was produced during the morning phase of the eruption; samples B3_b and B3_c were produced during the afternoon phase (B1 and B3 correlate with the fall characterization of Andrews and Gardner, 2009).

SFT descriptive parameters are plotted for the pumice, lithic, and crystal components of each sample (Fig. 6a–i). The first row of plots (Fig. 6a, d, g) represents the parameter distributions of pumice subpopulations, the second row (Fig. 6b, e, h) represents the distributions of lithic subpopulations, and the third row (Fig. 6c, f, i) represents the distributions of crystal subpopulations. *Mode* versus *weight percent* (Fig. 6a–c), *mode* versus *dispersion* (Fig. 6d–f), and *weight percent* versus *dispersion* (Fig. 6g–i) are plotted for each component. Multiple subpopulation points represent the component distribution of a single sample; for example, the pumice distribution of sample B1_a is characterized by four subpopulations, which translate to four sample points on the pumice component plots (Fig. 6a–c).

Mode versus *weight %* plots: We observe that despite significant differences in the component distributions of the three fallout samples (Table 2), the SFT parameters consistently display the same trends. The only exceptions to the sample clusters occur for weight percent
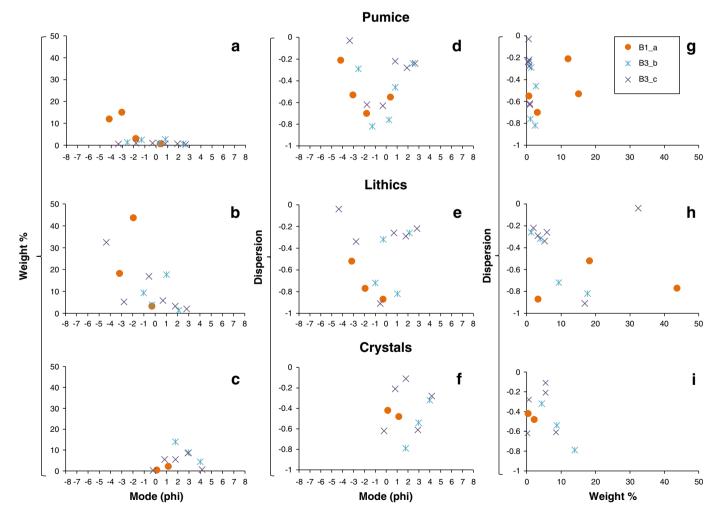

Fig. 6. SFT descriptive parameter data for the ash fall samples (ash fall sample relative componentry provided in Table 2; grain size and componentry data courtesy of Benjamin Andrews). The first row of plots (a, d, g) represents the parameter distributions of pumice subpopulations, the second row (b, e, h) represents the distributions of lithic subpopulations, and the third row (c, f, i) represents the distributions of crystal subpopulations. We plot mode versus weight percent (mode measured in phi; a–c), mode versus dispersion (d–f), and weight percent versus dispersion (g–i) for each component. Multiple subpopulation points represent the component distribution of a single sample.
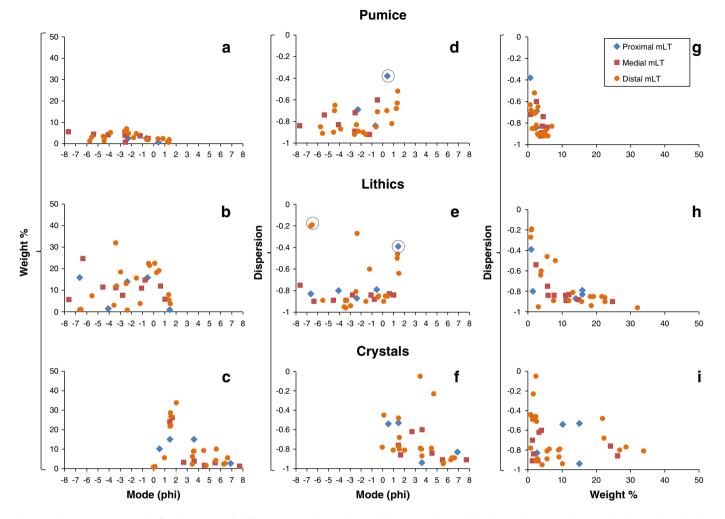
Fig. 7. SFT descriptive parameter data for the Unit III *mLT* lithofacies at proximal (<5.25 km), medial (5.25–7.25 km), and distal (>7.25 km) outcrop locations. The data are plotted in the same format as that used to present the ash fall data (ash fall SFT data presented in Fig. 6). For the travel distance plots, subpopulation points represent the component distributions of multiple samples for each outcrop distance. Outlying subpopulations that occupy very low (<1–2%) of the sample component distributions are circled.

values of subpopulations within samples that have a dominant component; for example, the B1_a subpopulations with high pumice weight percent values (Fig. 6a), and the B1_a and B3_c subpopulations with high lithic weight percent values (Fig. 6b).

Mode versus *dispersion* plots: The fallout samples display high average dispersion values for the coarse- and fine-grained subpopulations, with most points plotting between −0.4 and 0. However, there is an abrupt decrease in dispersion to values as low as −0.9 for the middle grain sizes. The trend is most apparent in the pumice and lithic components, for which the decrease in dispersion values occurs between −2 and 1 ϕ (Fig. 6d, e), and is present to a lesser degree in the crystal component data spread, for which the decrease in dispersion values occurs between −1 and 3 ϕ (Fig. 6f).

Weight % versus *dispersion* plots: All fallout samples show a general trend of decreasing dispersion values with increasing subpopulation weight percent (Fig. 6g–i). The outliers to this trend in the fallout distributions are the consequence of greater weight percent values for subpopulations describing dominant sample components (e.g., Fig. 6g for pumice, Fig. 6h for lithics). This trend also occurs in the SFT parameters of the other MSH lithofacies regardless of distance from source, and is discussed in greater detail in the following sections.

4.2.2. Travel distance data

To examine the impact of travel distance on PDC deposit SFT characteristics, we compare the parameter values for samples taken from the Unit III massive lapilli tuff (*mLT*) lithofacies at proximal (<5.25 km),

medial (5.25–7.25 km), and distal (>7.25 km) outcrop locations. SFT parameter data are plotted in the same format as that presented for the fall deposits (Fig. 7a–i). Multiple Unit III *mLT* samples were taken at each outcrop location and distance from source. As such, though individual samples may still be characterized by multiple subpopulations, the subpopulation points in the plots represent the component distribution of multiple samples for each outcrop distance.

Mode versus *weight %* plots: No significant changes are observed in the mode versus weight percent data for the pumice or lithic components with distance from source (Fig. 7a, b). The crystal component, however, shows a notable increase in weight percent between 1 Φ and 2 Φ, which correlates with the dominant MSH crystal size. There is also a more extensive distribution of the finest crystal sizes for medial and distal locations (Fig. 7c).

Mode versus *dispersion* plots: The pumice subpopulations in the mode versus dispersion plots show a general increase in dispersion with decreasing grain size at all outcrop locations (Fig. 7d). In contrast, the crystal subpopulations exhibit a moderate decrease in dispersion values for the smaller grain sizes, again at all outcrop locations (Fig. 7f). No changes in dispersion values as a function of grain size are observed for the lithic subpopulations (Fig. 7e).

We do not observe significant trends in the mode versus dispersion data for the pumice subpopulations with distance from source (Fig. 7d). The range of dispersion values for the lithic subpopulations increases with distance from source, from ~−0.9 to −0.7 for the proximal and medial locations to ~−0.9 to −0.2 for the distal locations; the average
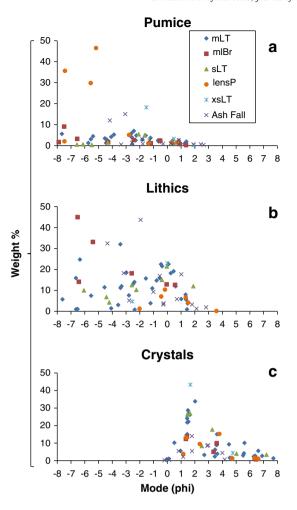
Fig. 8. Mode versus weight percent SFT data for the different MSH lithofacies (*mLT*, *mlBr*, *sLT*, *lensP*, *xsLT*, and ash fall); data series are identified by lithofacies. The upper plot represents the pumice component (a), the middle represents the lithics (b), and the lower represents the crystals (c). The subpopulation clusters represent multiple samples of each lithofacies.

Fig. 9. Mode versus dispersion SFT data for the different MSH lithofacies (*mLT*, *mlBr*, *sLT*, *lensP*, *xsLT*, and ash fall); data series are identified by lithofacies. The upper plot represents the pumice component (a), the middle represents the lithics (b), and the lower represents the crystals (c). The subpopulation clusters represent multiple samples of each lithofacies. Box plots depict the dispersion range and most populated zone (statistically constrained between the 1st and 3rd quartile) for each lithofacies; there are too few *xsLT* subpopulations to produce accurate quartile dispersion values so only the dispersion range is depicted.

lithic dispersion value is also highest at the most distal locations (Fig. 7e). Similar to the lithic component, we observe the greatest crystal subpopulation dispersion ranges for the distal samples, and the highest average crystal dispersion for the distal samples relative to the proximal and medial crystal samples (Fig. 7f).

Weight % versus *dispersion* plots: Similar to the trend observed in the fallout data plots, all Unit III *mLT* components show a distinct decrease in dispersion values with increasing subpopulation weight percent for all outcrop locations (Fig. 7g–i). This trend is most apparent for the lithic component, for which dispersion values range from ~−0.95 to −0.2 when weight fractions are less than 10%, but are limited to ~−0.95 to −0.8 when weight fractions are greater than 10% (Fig. 7h). A wide dispersion range for low weight fractions is also noted for the pumice component, but due to the consistently low weight percent of pumice subpopulations in the *mLT* the trend is not developed in the greater weight fractions (Fig. 7g). The crystal component displays the same general trend as the lithics, but a secondary cluster of subpopulations characterized by both greater weight fractions and higher dispersion values is also present (e.g., dispersion values from −0.8 to −0.6 for subpopulation weight percent >10%; Fig. 7i).

4.2.3. Lithofacies variation data

We examine the SFT parameter distributions for a variety of lithofacies to determine the extent to which parameter values reflect flow boundary conditions and emplacement processes as they are
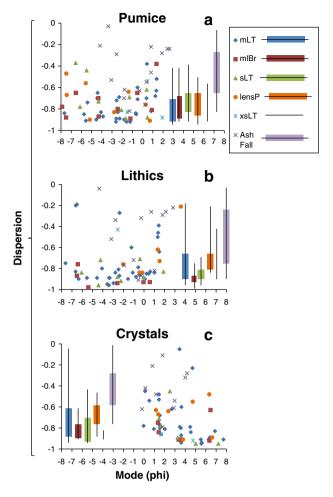
interpreted based on the previous work conducted on the extensive MSH deposit exposures (e.g., Bendana et al., 2012; Pollock and Brand, 2012; Pollock, 2013; Brand et al., in press). We examine massive lapilli tuff (*mLT*), massive tuff breccia (*mlBr*), stratified lapilli tuff (*sLT*), and pumice lens (*lensP*) lithofacies (Fig. 3; Table 1), as well as the proximal cross-stratified deposit (*xsLT*; Rowley et al., 1985; Beeson, 1987; Bendana et al., 2012) and the fallout samples studied in Fig. 6. The larger quantity of samples and component subpopulations results in graphical distributions that are significantly more complex for the lithofacies variation plots than for the fallout or travel distance plots. We plot the parameter data in the same format as that used to present the fall deposits and distance from source plots, but we separate the lithofacies plot columns into three figures in order to simplify the data spreads. As such, Fig. 8 plots *mode* versus *weight percent* for the three components, Fig. 9 plots *mode* versus *dispersion* for all three components, and Fig. 10 plots *weight fraction* versus *dispersion* for all three components. Data series are identified by lithofacies in the plot legend. As in the travel distance plots, the subpopulation clusters represent multiple samples of each lithofacies rather than a single lithofacies sample.

Mode versus *weight %* plots: The dominant components of the *lensP* and *mlBr* lithofacies (e.g., pumice in the *lensP*, lithics in the *mlBr*) display similar SFT parameter trends, in that the dominant component in the larger to medial size classes has greater weight percent values and
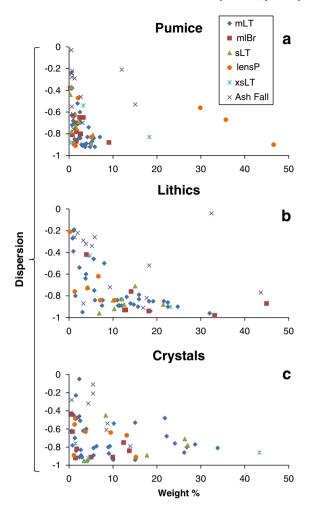
Fig. 10. Dispersion versus weight percent SFT data for the different MSH lithofacies (*mLT*, *mlBr*, *sLT*, *lensP*, *xsLT*, and ash fall); data series are identified by lithofacies. The upper plot represents the pumice component (a), the middle represents the lithics (b), and the lower represents the crystals (c). The subpopulation clusters represent multiple samples of each lithofacies.

broader dispersions for both lithofacies (Fig. 8a, b). We also observe diminished weight fractions of the non-dominant components in the *lensP* and *mlBr* for all size classes relative to the other lithofacies. The mode versus weight percent plot representing the crystal component further reveals that though the MSH pumice clasts are rich in crystals, the crystal component for the pumice lenses has low weight percent values relative to the other lithofacies in this study (Fig. 8c). The low crystal weight percent is most notable near the average crystal size (~1–2 ϕ), where the other lithofacies experience a peak in the crystal weight fraction. Finally, we observe that the SFT parameter distribution of the MSH *sLT* (observed and sampled at outcrop AD-3, Fig. 3), which grades laterally into *mLT*, is almost identical to the parameter distributions of all *mLT* samples (e.g., Fig. 8a–c).

Mode versus *dispersion* plots: We consider both the full range (from lowest dispersion value to highest for a given lithofacies) and most populated zone of subpopulation points when comparing the dispersion

Table 2
Relative componentry data for ash fall samples (unpublished data courtesy of Benjamin Andrews, Smithsonian Institute).

B1_a		B3_b		B3_c	
Pumice	31.22%	Pumice	11.94%	Pumice	4.46%
Lithics	66.21%	Lithics	47.58%	Lithics	72.82%
Crystals	2.57%	Crystals	20.48%	Crystals	22.72%

values exhibited across the different subpopulations for the MSH lithofacies. We use box plots in order to statistically simplify and describe the trends observed in the complex mode versus dispersion data produced by the SFT physical modeling. The box plots depict the dispersion range and most populated zone of dispersion data points (statistically constrained between the 1st and 3rd quartile) for each lithofacies, as overlain on the mode versus dispersion plots (Fig. 9). We note that there are too few *xsLT* subpopulations to produce accurate quartile dispersion values, and as such plot the dispersion range with no quartile box for this lithofacies. Most lithofacies occupy a fairly broad range of dispersion for all components. However, several significant differences between the component distributions and individual lithofacies are noted when both the quartile region and dispersion range data are examined.

The pumice component subpopulations of the *mLT*, *mlBr*, *sLT*, and *lensP* lithofacies are notably similar for both the full and quartile dispersion ranges, for all grain sizes (Fig. 9a). The entire dispersion spread for each of these lithofacies ranges from ~−0.9 to −0.4, and the quartile zone extends from ~−0.85 to −0.65. The pumice subpopulations of the *xsLT* also occupy the same data range. In comparison, the fallout lithofacies exhibits a more extended overall range (−0.82 to −0.03), and much higher dispersion values within the concentrated zone (−0.625 to −0.24) for the pumice component. A decrease in the dispersion values at the medial grain sizes for the pumice subpopulations, similar to the dip observed for the fallout samples (Fig. 6d–f), occurs for the *mLT*, *mlBr*, and *lensP* lithofacies between −4.5 to −1 Φ (Fig. 9a). This trend is not noted in the more dense lithofacies components.

The dispersion ranges of the lithic and crystal component distributions show more significant changes across the different lithofacies (Fig. 9b–c). The *mLT*, *mlBr*, and *sLT* subpopulations have similar concentrated dispersion ranges (~−0.9 to −0.6 or −0.7). The concentrated range for the *lensP* lithofacies encompasses slightly higher dispersion values (−0.82 to −0.6474), and the dispersion values characterizing the fallout quartile zone are significantly greater than the other lithofacies (−0.77 to −0.24). For the lithic and crystal component subpopulations, we observe that the range of dispersion values characterizing the quartile zone is generally the most broad for the *mLT* lithofacies (−0.89 to −0.6675 for lithics, Fig. 9b; −0.885 to −0.635 for crystals, Fig. 9c), and the most limited for the *mlBr* lithofacies (−0.9375 to −0.885 for lithics, Fig. 9b; −0.91 to −0.7725 for crystals, Fig. 9c). We also note that the crystal component subpopulations have the highest overall dispersion values for all lithofacies (~−0.8 to −0.2 for crystals, compared with ~−0.95 to −0.7 for lithics and −0.9 to −0.65 for pumice; Fig. 9a–c).

Weight % versus *dispersion* plots: The trend of decreasing dispersion values with increasing subpopulation weight percent observed for the fallout and Unit III *mLT* samples is present for each component, for all of the MSH lithofacies (weight fraction versus dispersion plots, Fig. 10). The trend is least developed in the pumice component (Fig. 10a). For the pumice subpopulations, dispersion values range from ~−0.98 to −0.1 for all lithofacies when weight fractions are less than 10%, but weight percent values are rarely greater than 6 or 7% so any trend with increasing weight percent is not developed. The outlying points in the pumice component plots are from samples with high pumice content (e.g., *lensP* and the pumice-rich fallout sample; Table 2).

The lithic component expresses the trend of decreasing dispersion with increasing subpopulation weight percent most distinctly for all lithofacies (Fig. 10b). Dispersion values range from ~−0.99 to −0.2 for weight fractions less than 10%, and the dispersion range is limited to ~−0.99 to −0.7 or less when weight fractions are greater than 10%. There are only three outlying points in the lithic component plot, all from the fallout samples with significantly high lithic contents (Table 2).

Again, both the general trend of decreasing dispersion values with increasing subpopulation weight percent and the secondary cluster of subpopulations exhibiting greater weight fractions and higher dispersion values characterize the crystal subpopulations for all MSH

lithofacies (Fig. 10c). Dispersion values range from ~−0.95 to −0.4 when subpopulation weight percent values are greater than 10% in the crystal component, though the range decreases to ~−0.9 to −0.7 for crystal subpopulations with weight percent greater than 25%.

5. Discussion

Different PDC particle transport mechanisms have been shown to produce unique size–density distributions at the outcrop scale, enabling the reconstruction of parent current processes using physically-based SFT model functions and descriptive parameters (e.g., Wohletz et al., 1989; Orsi et al., 1992; Wohletz and Raymond, 1993; Wohletz and Brown, 1995; Wohletz et al., 1995; Wohletz, 1998; Taddeucci and Palladino, 2002). We interpret the SFT data trends described above in terms of particle transport mechanisms and depositional conditions, and examine the extent to which the deposit information provided using SFT analysis coincides with the field observations and interpretations made based on the excellent MSH deposit exposures (e.g., Pollock and Brand, 2012; Pollock, 2013; Brand et al., in press). Our evaluation of the SFT results for the fallout, travel distance, and lithofacies comparison studies within the context of broader MSH field observations allows us to further define and reinforce the capabilities of SFT analysis when applied to pyroclastic deposits, and to develop a more complete understanding of PDC dynamics based on the detailed particle size–density trends characterized by the SFT parameters.

5.1. Fallout

The same SFT parameter trends are observed for the fallout samples despite the differences in initial ash fall componentry and grain size distributions (Table 2). This suggests that the SFT approach strongly reflects particle transport mechanisms, and that the general SFT parameter distributions are (to some degree) independent from the specific component distributions of individual pyroclastic samples. We note that the pumice subpopulation outliers for sample B1_a (e.g., Fig. 6a, g) and lithic outliers for sample B3_c (e.g., Fig. 6b, h) certainly reflect the higher initial weight percent values of these components within each fallout sample. However, the pumice outliers in B1_a may also reflect density variations in the individual pumice clasts that our density study does not account for.

The decrease in dispersion values in the middle size range for all components suggests more poorly-sorted and less processed subpopulations relative to the coarser and finer grain sizes. Previous work by Durant et al. (2009) applied SFT analysis to MSH fallout deposits at distances ~100 to 700 km from source and observed ash particle aggregation at these locations, which results in substantially increased particle processing and high (>0) dispersion values for the relevant grain sizes. Particle aggregation was not noted in the proximal fallout sample locations examined in our study, and we observe that fragmentation mechanisms do not impact MSH component subpopulations as ubiquitously as individual transport processes. As such, because the decrease in dispersion occurs for all components in the middle grain sizes it likely relates to a transport process rather than aggregation or fragmentation mechanisms. The higher dispersion values for the finer and coarser grain sizes may reflect that the particles comprising these subpopulations are more influenced by suspension or turbulent drag, while the decreased dispersion values in the middle size range likely reflect ballistic transport with limited turbulence or drag effects.

5.2. Travel distance

Conventional grain size and fabric studies reveal limited change within the Unit III *mLT* lithofacies with distance from source. There is little decrease in median grain size or increase in degree of sorting with distance, and the unit has a relatively high quantity of fine ash for the

MSH *mLT* lithofacies at all locations across the pumice plain. As previously interpreted, the lack of fines depletion or pumice lenses, the random (rather than concentrated) distribution of lithic blocks, and the absence of conventional fining or sorting trends with distance from source suggest that Unit III was deposited from a highly concentrated current with suppressed density segregation and elutriation. The lack of significant change in the mode versus weight percent SFT parameter distributions for the pumice and lithic components more specifically indicates that there was little change in the Unit III grain size distributions for these components during transport. However, the detailed examination provided by the analysis of additional SFT parameters and PDC components reveals changes in the Unit III particle characteristics that are not observed in the conventional grain size and fabric data, and indicates that size–density segregation did occur within the current during transport.

In their study of pyroclastic particle size–density relationships, Taddeucci and Palladino (2002) find that the SFT parameters describing the crystal subpopulations are better indicators of particle emplacement processes than the pumice or lithic subpopulations, and contend that this is due to the initial homogeneity of crystal size and density relative to the pumice and lithic components. For the MSH deposits, we are able to elucidate emplacement and transport information from the pumice and lithic subpopulations as well as the crystal subpopulations. However, we note that the greater size–density constraints on the crystal component may allow us to isolate the SFT parameter distributions and resulting interpretations from the influence of complex initial particle distributions such as those characterizing the pumice and lithics.

The weight percent increase in the crystal component subpopulations around 1 Φ reflects the initial size constraints on the crystal component. The dominant crystal size from the May 18, 1980 magma is ~1 Φ, resulting in an increased weight percent of the ~1 Φ crystal subpopulations (Fig. 7c). The greater number of relatively fine-grained crystal subpopulations at the medial and distal outcrop locations is a consequence of crystal fracturing and fragmentation during transport.

For all Unit III outcrop locations, the smaller grain sizes of the pumice component have higher dispersion values (Fig. 7d), while the larger grain sizes of the crystal component have lower dispersion values (Fig. 7f). The trend in the pumice component reflects a transport or fragmentation mechanism that processes smaller grain sizes to a greater degree than the larger grain sizes, regardless of deposit distance from source. The trend of better sorting for larger crystal sizes is consistent with the aforementioned initial size range of intact crystals. Crystal size is limited by the degree of crystal growth (reflected as crystal aggregation in the SFT program) as well as the degree of crystal fragmentation or break-up during transport. Other than necessarily occupying smaller size bins than the parent crystals, crystal fragments do not have initial size constraints that influence the component distribution. As such, the larger crystal grain sizes (made up of primarily whole crystals) are more constrained and processed, while the smaller crystal grain sizes (made up of primarily crystal fragments) are not constrained and are relatively poorly processed.

The higher average dispersion values observed for the lithic and crystal components at distal outcrop locations relative to the proximal and medial distributions suggests that these components were notably influenced by segregation and processing mechanisms with distance from source, possibly as a result of their greater densities. Additionally, the greater dispersion ranges for the lithics and crystals at distal locations indicate that these denser components experienced more complex processing mechanisms during transport (Fig. 7e, f).

5.3. Lithofacies variation

Stratigraphic analysis and the study of lithofacies architectures provide valuable information and limits on local PDC flow boundary processes and deposit emplacement mechanisms (e.g., Walker, 1971; Sparks, 1976; Valentine et al., 1992; Wohletz, 1998; Branney and Kokelaar,

2002; Taddeucci and Palladino, 2002; Sulpizio et al., 2008). Previous studies at MSH have been able to constrain PDC flow boundary conditions with distance from source, over a variety of substrate and surface roughness conditions (Pollock and Brand, 2012; Brand et al., in press). The application of SFT methodology to the well-constrained MSH PDC deposits allows us to examine how SFT parameters reflect current processes and flow boundaries. Furthermore, when we consider both the deposit characteristics and the detailed particle distribution analysis that SFT provides, we are able to make significant interpretations regarding regional PDC sedimentation regimes.

We note that the dominant components of the *lensP* and *mlBr* lithofacies have significantly different densities (pumice density ranges from 730 to 1370 kg m^{-3}; lithic density is approximately 2700 kg m^{-3}) and particle characteristics (pumice clasts are rounded; lithics are angular to subrounded). The comparable SFT parameter trends observed for the *lensP* and *mlBr* (Fig. 8a, b) indicate that despite their different component and density characteristics, pumice lenses and lithic breccias are produced and sustained by similar transport and density-segregation processes acting within the flow boundary region.

The weight percent values of the crystal component within the *lensP* lithofacies reflect both sorting mechanisms and the level of particle collision energy present in the pumice lenses during transport and deposition (Fig. 8c). The low crystal weight percent relative to the other lithofacies is consistent with the interpretation that pumice lenses are the result of density segregation and pumice rafting processes within PDCs, concentrating low-density pumice clasts at equal density interfaces while segregating the denser particles into the surrounding current (e.g., Druitt, 1995; Calder et al., 2000; Rowley et al., 2012). The low quantity of crystals within the pumice lenses may also indicate (1) that pumice–pumice collisional energy is not great enough to free crystals from the pumice glass matrix, (2) that the duration of pumice–pumice collision is not extended enough to free crystals during transport, or (3) that lithic–pumice collision is required to free the crystals from the glass matrix, and consequentially lithic–pumice interactions produce the volume of free crystals observed in the deposits. This is further supported by the observation that pumice within the massive PDC deposits and pumice lenses are consistently found at maximum roundness within both flow Units III and IV at all distances across the pumice plain (Brand et al., in press). This suggests that abrasion and comminution occurred in the energetic proximal regions (i.e., steep flanks) before the PDCs entered the pumice plain consistent with the findings of Manga et al. (2011), and that even though the currents were likely concentrated and particle–particle collisions important, particle collisional energy was not sufficient to break the pumice because the pumice is not observed to decrease in roundness.

The nearly identical parameter distributions for the *mLT* and *sLT* lithofacies (Fig. 8) indicate that SFT analysis can be used to distinguish local current instabilities from regional transport processes. The deposit exposure at MSH allows us to determine that the stratified deposit sampled for this study was produced by a local instability within a concentrated current that left predominantly massive deposits as it traveled across the pumice plain. The SFT parameter distributions of the *mLT* and *sLT* indicate that the deposits were produced by similar transport and depositional processes despite the different characteristics observed at the outcrop scale; the SFT results do not reflect the local instability that produced the *sLT*. These findings are consistent with previous work that suggests that the SFT analysis of particle size–density relationships is more representative of regional transport conditions than of local depositional processes (e.g., Wohletz et al., 1989, 1995; Wohletz, 1998; Taddeucci and Palladino, 2002).

Previous applications of SFT analysis to pyroclastic deposits have attributed depositional conditions and flow boundaries to specific SFT dispersion values and mode ranges (e.g., Orsi et al., 1992; Wohletz, 1998). These studies focus on four major transport processes (ballistic, suspension, saltation, and traction), and characterize bulk sample distributions using SFT. We are not able to confidently connect specific SFT parameter

values with transport mechanisms for the MSH component subpopulations in this study. However, we do observe trends in the relative dispersion ranges and areas of high subpopulation concentration for each lithofacies, as depicted in the box plots in Fig. 9 (high subpopulation concentration is statistically defined as the zone between the 1st and 3rd quartile for individual lithofacies) and interpreted below. We note that most of our observations are consistent with expectations based on the emplacement mechanisms indicated by deposit characteristics.

The higher dispersion values for the fallout lithofacies for the pumice, lithic, and crystal components (Fig. 9) indicate that all of the components are more thoroughly processed and better sorted relative to the components of the other lithofacies. This is expected since fallout samples are the product of suspension sedimentation processes, as opposed to the other lithofacies which are produced by dilute or concentrated PDCs. These MSH SFT parameter results are consistent with established trends in pyroclastic deposits (e.g., Walker, 1971; Sparks et al., 1973; Sheridan et al., 1987; Branney and Kokelaar, 2002; Taddeucci and Palladino, 2002). The lithic and crystal subpopulations within the *lensP* lithofacies demonstrate the next highest dispersion values after the fallout samples (Fig. 9b, c). The high dispersion values indicate better sorting and more complete processing of the dense components within the *lensP*, consistent with previous interpretations of *lensP* density segregation processes (e.g., Druitt, 1995; Calder et al., 2000).

The *mlBr* subpopulations consistently have the lowest dispersion values and most limited dispersion range, data that indicates the *mlBr* is the most poorly-sorted and least processed of the MSH lithofacies (Fig. 9a–c). This suggests that once the particles are segregated into a concentrated zone of lithics, further processing, sorting, and segregation are inhibited. We note that the breccia in our study was transported from the vent rather than locally entrained, and as such the poor sorting and processing is not a result of limited particle travel distance.

The PDC conditions that result in the decrease in pumice subpopulation dispersion values at the medial grain sizes for the *mLT*, *mlBr*, and *lensP* lithofacies (Fig. 9a) are likely the same as the conditions producing the trend in all components within the fallout lithofacies (discussed in Section 5.1 *Fallout*, Fig. 6d–f). As such, the decreased suspension or turbulent drag effects that we interpret to be responsible for the dip in dispersion values in the middle size range occur throughout a wide range of transport regimes.

The trend of decreasing dispersion values with increasing subpopulation weight percent for all PDC deposit components (Fig. 10a–c) reflects a process that occurs for all lithofacies, regardless of distance from source. The smaller subpopulations (e.g., those that occupy lesser distribution weight percent) have broader ranges of dispersion values; that is, the smaller subpopulations undergo a greater variety of transport or fragmentation processes. This is plausible in that there may be a large number of minor transport or fragmentation mechanisms influencing the particles within the current, but major mechanisms affecting a greater quantity of current components are more limited.

For the lithofacies variation plots, the only outliers in the decreasing dispersion with increasing weight percent trend occur for subpopulations representing the dominant component of a sample or lithofacies, and reflect the greater weight percent of that dominant component (Fig. 10a–c). The outliers have higher dispersion values for larger weight percent than the general trend, which reflects greater particle processing. This is consistent with what is expected for particle processing: if there is a dominant component in a current, it undergoes a greater degree of processing within that current than the components that do not occupy such a large percent of the PDC solid fraction.

As we mention regarding the fallout and travel distance plots, the lithic and crystal components are more influenced by the transport mechanism and parameter relationship that produces the decreasing dispersion with increasing subpopulation weight percent trend than the other components. The crystals and lithics are of similar density, which suggests that density influences the extent to which particles are processed by the affecting mechanism. The pumice may not show

the relationship to such an extent because of the low weight percent of the pumice component in the *mLT* deposit samples. The limited trend for the pumice component may also be due to density difference or segregation that does not impact the pumice clasts in the same way as the lithics and crystals.

The crystals show the same trend as the lithics, with an additional cluster of subpopulation points that demonstrate greater dispersion values for larger weight fractions (Fig. 10c). We interpret that the secondary trend relates to the initial size constraints on the crystal component, which result in inherently better sorting and enhanced processing for the crystals than for the other components.

6. Conclusion

The extensive PDC deposit exposures at MSH provide accurate constraints on PDC regimes and flow boundary conditions at specific locations across the pumice plain, and enable a detailed and controlled examination of the size–density and SFT parameter relationships exhibited by pyroclastic deposit components. The application of the physically-based SFT methodology to the well-constrained MSH deposits suggests that SFT parameter distributions can be effectively used to characterize flow boundary conditions and emplacement processes for a variety of PDC lithofacies and deposit locations. Additionally, this study's integration of field observations and detailed SFT particle distribution analysis allow us to make interpretations regarding PDC dynamics and flow boundary processes.

The comparison of MSH fallout samples confirms that the SFT approach strongly reflects particle fragmentation and transport mechanisms, independent of the initial component distributions of pyroclastic samples. SFT analysis of the Unit III *mLT* provides evidence for density segregation within the current and reveals changes in particle characteristics with distance from source that are not observed in the conventional grain size data. These findings suggest that the SFT methodology provides significantly more information about flow dynamics and processes within the parent current than conventional PDC study methods (e.g., Wohletz et al., 1989; Orsi et al., 1992; Brown and Wohletz, 1995; Taddeucci and Palladino, 2002). The nearly identical *mLT* and *sLT* SFT parameter distributions also validate previous work. The comparable *mLT* and *sLT* parameter results do not reflect the local current instability that produced the *sLT*, and confirm that SFT analysis of particle size–density relationships is more representative of regional transport conditions than local (outcrop-scale) depositional processes (e.g., Wohletz et al., 1989; Wohletz, 1998; Taddeucci and Palladino, 2002).

Integrated MSH field observations and SFT analysis provide in-depth information regarding PDC sedimentation regimes and particle segregation mechanisms. Most notably, the comparable SFT parameter trends for the *lensP* and *mlBr* lithofacies indicate that despite the different density and shape characteristics of the constituent components, pumice lenses and lithic breccias are produced and sustained by similar density-segregation processes acting within the current. Additionally, the low weight percent values of the crystal subpopulations in the *lensP* relative to the other lithofacies reflect both sorting mechanisms and the particle collision energy present within the pumice lenses. The lesser quantity of crystals is consistent with the interpretation that high-density particles are segregated out of low-density pumice lenses into the surrounding current, and may also suggest (1) that pumice–pumice collisional energy is not great enough to free crystals from the pumice glass matrix, (2) that the duration of pumice–pumice collision is not long enough to free crystals during transport, or (3) that lithic–pumice collision is necessary to free crystals from the glass matrix and produce the volume of free crystals observed in the deposits (Druitt, 1995; Calder et al., 2000; Rowley et al., 2012).

The relative dispersion ranges and areas of concentrated dispersion data points for each lithofacies do show processing trends that are consistent with expectations based on the emplacement mechanisms indicated by deposit characteristics (e.g., Walker, 1971; Branney and

Kokelaar, 2002). Additionally, the trend of decreasing dispersion values with increasing subpopulation weight percent observed for all PDC deposit components is consistent with intuitive expectations for particle processing mechanisms: there may be a number of minor transport or fragmentation mechanisms that influence lesser, lower weight percent subpopulations, but the mechanisms affecting greater weight percent of current components are more limited, resulting in a narrower range of dispersion values and decreased overall processing.

The size–density and SFT parameter relationships we observe at MSH can be used to effectively characterize regional transport processes, and when combined with field observations the SFT data provides valuable information about PDC segregation and particle processing mechanisms. This study further defines and reinforces the capabilities of SFT analysis when applied to pyroclastic deposits, and demonstrates that SFT methodology has the potential to constrain regional flow boundary conditions at field sites where outcrop exposures are limited.

References

Allen, S.R., 2001. Reconstruction of a major caldera-forming eruption from pyroclastic deposit characteristics: Kos Plateau Tuff, eastern Aegean Sea. J. Volcanol. Geotherm. Res. 105, 141–162.

Andrews, B.J., Gardner, J.E., 2009. Turbulent dynamics of the 18 May 1980 Mount St. Helens eruption column. Geology 37, 895–898.

Beeson, D.L., 1987. Proximal Flank Facies of the May 18, 1980 Ignimbrite: Mount St Helens, Washington. University of Texas at Arlington (MS Thesis).

Bendana, S., Brand, B.D., Self, S., Dufek, J., 2012. Effects of slope on the dynamics of dilute pyroclastic density currents from May 18th, 1980 Mt. St. Helens eruption. American Geophysical Union Annual Meeting (Abstract V41B-2778).

Bourdier, J.L., Abdurachman, E.K., 2001. Decoupling of small-volume pyroclastic flows and related hazards at Merapi volcano, Indonesia. Bull. Volcanol. 63, 309–325.

Brand, B.D., Mackaman-Lofland, C., Pollock, N., Bendana, S., Dawson, B., Wichgers, P., 2014. Dynamics of pyroclastic density currents: conditions that promote substrate erosion and self-channelization—Mount St Helens, Washington (USA). J. Volcanol. Geotherm. Res. http://dx.doi.org/10.1016/j.jvolgeores.2014.01.007 (in press).

Branney, M.J., Kokelaar, B.P., 2002. Pyroclastic density currents and the sedimentation of ignimbrites. Geol. Soc. London Mem. 27 (143).

Brown, W.K., Wohletz, K.H., 1995. Derivation of the Weibull distribution based on physical principles and its connection to the Rosin–Rammler and lognormal distributions. J. Appl. Phys. 78, 2758–2763.

Burgisser, A., Bergantz, G.W., 2002. Reconciling pyroclastic flow and surge: the multiphase physics of pyroclastic density currents. Earth Planet. Sci. Lett. 202, 405–418.

Calder, E.S., Sparks, R.S.J., Gardeweg, M.C., 2000. Erosion, transport and segregation of pumice in pyroclastic flows inferred from ignimbrite at Lascar Volcano, Chile. J. Volcanol. Geotherm. Res. 104, 201–235.

Christiansen, R.L., Peterson, D.W., 1981. Chronology of the 1980 eruptive activity. In: Lipman, P.O., Mullineaux, D.R. (Eds.), The 1980 Eruptions of Mount St. Helens, Washington. US Geological Survey Professional Paper 1250, pp. 17–30.

Criswell, C.W., 1987. Chronology and pyroclastic stratigraphy of the May 18, 1980 eruption of Mount St. Helens, Washington. J. Geophys. Res. 92, 10237–10266.

Dellino, P., De Astis, G., La Volpe, L., Mele, D., Sulpizio, R., 2011. Quantitative hazard assessment of phreatomagmatic eruptions at Vulcano (Aeolian Islands, Southern Italy) as obtained by combining stratigraphy, event statistics and physical modeling. J. Volcanol. Geotherm. Res. 201, 364–384.

Druitt, T.H., 1995. Settling behavior of concentrated dispersions and some volcanological applications. J. Volcanol. Geotherm. Res. 65, 27–39.

Druitt, T.H., Avard, G., Bruni, G., Lettieri, P., Maez, F., 2007. Gas retention in fine-grained pyroclastic flow materials at high temperatures. Bull. Volcanol. 69, 881–901.

Durant, A.J., Rose, W.I., Sarna-Sojcicki, A.M., Carey, S., Volentik, A.C.M., 2009. Hydrometeor-enhanced tephra sedimentation: constraints from the 18 May 1980 eruption of Mt. St. Helens. Journal of Geophysical Research 114 (B03204).

Fisher, R.V., 1990. Transport and deposition of a pyroclastic surge across an area of high relief: the 18 May 1980 eruption of Mount St. Helens, Washington. Geological Society of America, Bulletin 102 1038–1054.

Francis, P., 1993. Volcanoes — a planetary perspective. Oxford University Press Inc., New York.

Giordano, G., 1998. The effects of paleotopography on lithic distribution and facies associations of small volume ignimbrites: the WTT Cupa (Roccamonfina volcano, Italy). J. Volcanol. Geotherm. Res. 87, 255–273.

Kieffer, S.W., 1981. Fluid dynamics of the May 18 blast at Mount St. Helens. In: Lipman, P.O., Mullineaux, D.R. (Eds.), The 1980 Eruptions of Mount St. Helens, Washington — US Geological Survey Professional Paper 1250, pp. 379–400.

Kuntz, M.A., Rowley, P.D., MacLeod, N.S., Reynolds, R.L., McBroome, L.A., Kaplan, A.M., Lidke, D.J., 1981. Petrography and particle–size distribution of pyroclastic-flow, ash-cloud, and surge deposits. In: Lipman, P.O., Mullineaux, D.R. (Eds.), The 1980 Eruptions of Mount St. Helens, Washington. US Geological Survey Professional Paper 1250, pp. 525–539.

Manga, M., Patel, A., Dufek, J., 2011. Rounding of pumice clasts during transport: field measurements and laboratory studies. Bull. Volcanol. 73, 321–333.

Orsi, G., Gallo, G., Heiken, G., Wohletz, K., Yu, E., Bonani, G., 1992. A comprehensive study of pumice formation and dispersal: the Cretaio Tephra of Ischia (Italy). J. Volcanol. Geotherm. Res. 53, 329–354.

Pollock, N., Brand, B., 2012. Investigation into the erosive capacity of pyroclastic density currents at Mount Saint Helens, Washington (USA). American Geophysical Union Annual Meeting (Abstract V54C-01).

Pollock, N., 2013. Field Evidence for Substrate Entrainment by Pyroclastic Density Currents and its Effect on Downstream Dynamics at Mount St. Helens, Washington (USA). University of Washington (M.S. Thesis).

Roche, O., 2012. Depositional processes and gas pore pressure in pyroclastic flows: an experimental perspective. Bull. Volcanol. 74, 1807–1820.

Rowley, P., Kokelaar, P., Menzies, M., Waltham, D., 2012. Shear-derived mixing in dense granular flow. J. Sediment. Res. 81, 874–884.

Rowley, P.D., Kuntz, M.A., MacLeod, N.S., 1981. Pyroclastic-flow deposits. US Geological Survey Professional Paper 250 489–512.

Rowley, P.D., Macleod, N.S., Kuntz, M.A., Kaplan, A.M., 1985. Proximal bedded deposits related to pyroclastic flows of May 18, 1980, Mount St Helens, Washington. Geol. Soc. Am. Bull. 96, 1373–1383.

Sheridan, M.F., Wohletz, K.H., Dehn, J., 1987. Discrimination of grain-size subpopulations in pyroclastic deposits. Geology 15, 367–370.

Sparks, R.S.J., 1976. Grain size variations in ignimbrites and implications for the transport of pyroclastic flows. Sedimentology 23, 147–188.

Sparks, R.S.J., Bursik, M.I., Carey, S.N., Gilbert, J.S., Glaze, L.S., Sigurdsson, H., Woods, A.W., 1997. Volcanic Plumes. John Wiley, Chichester.

Sparks, R.S.J., Self, S., Walker, G.P.L., 1973. Products of ignimbrite eruptions. Geology 1, 115–118.

Sulpizio, R., De Rosa, R., Donato, P., 2008. The influence of variable topography on the depositional behavior of pyroclastic density currents: the examples of the Upper Pollara eruption (Salina Island, southern Italy). J. Volcanol. Geotherm. Res. 175, 3367–3385.

Taddeucci, J., Palladino, D.M., 2002. Particle size–density relationships in pyroclastic deposits: inferences for emplacement processes. Bull. Volcanol. 64, 273–284.

Taddeucci, J., Wohletz, K.H., 2001. Temporal evolution of the Minoan eruption (Santorini, Greece), as recorded by its Plinian fall and interlayered ash flow deposits. J. Volcanol. Geotherm. Res. 109, 301–319.

Valentine, G.A., 1998. Damage to structures by pyroclastic flows and surges, inferred from nuclear weapons effects. J. Volcanol. Geotherm. Res. 87, 117–140.

Valentine, G.A., Wohletz, K.H., Kieffer, S.W., 1992. Effects of topography on facies and compositional zonation in caldera-related ignimbrites. Geol. Soc. Am. Bull. 104, 154–165.

Walker, G.P.L., 1983. Ignimbrite types and ignimbrite problems. J. Volcanol. Geotherm. Res. 17, 65–88.

Walker, G.P.L., 1971. Grain-size characteristics of pyroclastic deposits. Geology 79, 696–714.

Wohletz, K.H., 1998. Pyroclastic surges and compressible two-phase flow. In: Freundt, A., Rosi, M. (Eds.), From Magma to Tephra — Modelling Physical Processes of Explosive Volcanic Eruptions. Developments in Volcanology. Elsevier, pp. 247–312.

Wohletz, K., Brown, W., 1995. Particulate size distributions and sequential fragmentation/transport theory. In: Theofanous, A., Akiyama, M. (Eds.), Intense Multiphase Interactions. Proceedings of US (NSF) Japan (JSPS) Joint Seminar, Santa Barbara CA. June 8–13 1995, pp. 235–241.

Wohletz, K., Orsi, G., de Vita, S., 1995. Eruptive mechanisms of the Neapolitan Yellow Tuff interpreted from stratigraphic, chemical, and granulometric data. J. Volcanol. Geotherm. Res. 67, 263–290.

Wohletz, K.H., Sheridan, M.F., Brown, W.K., 1989. Particle-size distributions and the sequential fragmentation/transport theory applied to volcanic ash. J. Geophys. Res. 94, 15703–15721.

Wohletz, K.H., Raymond, R., 1993. Atmospheric dust dispersal analyzed by granulometry of the Misers Gold event. J. Geophys. Res. 98, 557–566.